



Cite this: *RSC Adv.*, 2020, **10**, 6973

Received 21st December 2019
 Accepted 7th February 2020

DOI: 10.1039/c9ra10772j
rsc.li/rsc-advances

The influence of dopants on aW-phase antimonene: theoretical investigations

Qingxiao Zhou, ^{a*}ab Qian Zhang,^a Weiwei Ju,^a Yanling Liu^a and Jiahui Li^a

We systematically investigate the effect of dopants on the geometrics, electronic and magnetic properties of asymmetric washboard structure of antimonene (aW-Sb) by using density functional theory (DFT) calculations. The large binding energies and short bond lengths indicate the doped systems still maintain high stability. Pristine aW-Sb is a nonmagnetic semiconductor with a narrow band gap, while the doped aW-Sb exhibit metallic by doping. Furthermore, the Ti, V, Cr, Mn and Fe doping induced magnetic states, and the result of spin density indicates that the magnetic moments are mainly localized at dopant and the adjacent Sb atoms.

1. Introduction

Two-dimensional (2D) materials, such as graphene, transition metal dichalcogenides (TMDs), phosphorene, and silicene, have attracted considerable attention because of their intriguing mechanical, electronic, optical and thermal properties,^{1–6} which has led to these 2D materials being promising for new optoelectronic and nanoelectronic applications.^{7–10} Recently, antimonene, a monolayer of antimony, was predicted to exhibit a stable geometry and be a semiconductor by density functional theory (DFT).¹¹ Subsequently, monolayer antimonene has been experimentally achieved on Bi₂Te₃ (111), Sb₂Te₃ (111),¹² or PdTe₂ (ref. 13) substrates. Furthermore, an asymmetric washboard structure of antimonene (aW-Sb) was found to maintain its stability at a high temperature of 1000 K, and its armchair and zigzag nanoribbons exhibit excellent electronic properties.

Currently, for the exploration of 2D materials, doping is an effective method to achieve anticipant properties.^{14–20} Dai *et al.*²¹ investigated the effect of Fe-dopants on β -phase antimonene and found that the Fe-doped system exhibited stable room temperature ferromagnetism (RTFM). He *et al.*²² and Zhou *et al.*²³ reported 3d transition metal (TM) doped β -phase antimonene, and the results suggested that the doped systems were magnetic semiconductors. Li *et al.*²⁴ found that electric field and dopants improved the sensitivity to CO molecules of β -antimonene. Yang *et al.*^{25,26} investigated the effect of vacancies and 3d-transition-metal doped β -antimonene, and the results indicated that different vacancies and 3d-dopants resulted in

different electronic structures and magnetic properties in antimonene. However, few studies explored the effect of dopants on the electronic and magnetic properties of aW-phase antimonene.

Therefore, in this work, we aim to systematically explore the effect of dopants (Ge, Se, Sn, Te, Sc, Ti, V, Cr, Mn, Fe, Co, and Ni) on the properties of aW-phase antimonene using DFT calculations. Firstly, we examined the stabilities of doped systems by calculating the binding energies, charge transfer, and bond lengths. Secondly, we investigated the change of electronic structures. Finally, the magnetic behaviors of doped systems were explored. We hope our results could provide useful information for designing new antimonene-based magnetic and electronic devices.

2. Calculation details and models

All calculations were done with the Vienna *ab initio* Simulation Package (VASP).^{27–29} The generalized gradient approximation (GGA) using Perdew–Burke–Ernzerhof (PBE) parameterization was used to approximate the exchange-correlation potential,³⁰ and the Projector-Augmented Wave (PAW) pseudopotentials were employed.³¹ A plane-wave basis set with the kinetic energy cutoff is 500 eV and the van der Waals (vdW) was carried out by D3–Grimme correction (DFT-D3).³² Considering the localization of 3d TM-dopants, GGA+U is adopted to describe the strong on-site Coulomb interaction. Moreover, the spin-orbit couplings (SOC) act important role in the band structures^{33,34} and is also included to calculated the band structures in our study. The convergence criterion between two consecutive steps was set as 10^{-6} eV and a maximum force of 0.001 eV \AA^{-1} was allowed on each atom. A $8 \times 8 \times 1$ *k*-point sampling was used for $4 \times 4 \times 1$ antimonene supercells. A vacuum space of 15 \AA was set along the out-of-plane direction to avoid the interactions between the neighboring layers. To

^aCollege of Physics and Engineering, Henan University of Science and Technology, Luoyang 471023, People's Republic of China. E-mail: zhouqingxiao1989@163.com; Tel: +86 18567628290

^bHenan Key Laboratory of Photoelectric Energy Storage Materials and Applications, Henan University of Science and Technology, Luoyang 471023, People's Republic of China



explore the stability of doped systems, the binding energy (E_b) for the doped systems, as follows:

$$E_b = E_{\text{doped-Sb}} - E_{\text{V-Sb}} - E_{\text{dopant}} \quad (1)$$

where $E_{\text{doped-Sb}}$ represents the total energy of the doped antimonene, and $E_{\text{V-Sb}}$ is the energy of antimonene with a single vacancy, and E_{dopant} is the energy of an isolated dopant atom, respectively.

3. Results and discussion

3.1 Geometry structures

Our optimized model of aW-phase antimonene (aW-Sb) is performed in Fig. 1(a) and (b). The lattice constants of a_1 and a_2 are calculated to be 4.28 Å and 4.77 Å, and the nearest-neighbor distances b_1 and b_2 are 2.93 Å and 2.87 Å, respectively. The calculated parameters of geometry structure of aW-Sb are well agreement with previous literatures.^{35,36} According to previous reports, aW-Sb is a semiconductor with narrow bandgaps. The band structure of aW-Sb is described in Fig. 1(c). It can be found that it exhibits a indirect band gap of 0.12 eV, which is consistent with previous PBE results.^{37,38} We also calculated the bandgap by HSE correction (PBE + HSE) and spin-orbit

couplings method (PBE + SOC), and the values are 0.33 eV and 0.03 eV, and the HSE results is larger than PBE result. The SOC result is smaller than PBE result, which is due to the valence band near Y-point splits into two bands. Furthermore, the spin-up (majority) and spin-down (minority) channel are represented by black and blue color lines, which are completely symmetrical and the PBE band result is blue color. It suggests the aW-Sb is nonmagnetic. To examine the stability of aW-Sb, the phonon dispersion curves are shown in Fig. 1(d). It can be observed that no imaginary vibrating modes exist, and that illustrates the stability as monolayer antimonene.

To systematically explore the influence of dopant on aW-Sb, we consider 10 types of dopants, including Ge, Se, Sn, Te, Sc, Ti, V, Cr, Mn, Fe, Co, and Ni. The doped aW-Sb structure was created by replacing a Sb atom by a dopant atom, and the doping concentration is 1.56%. Furthermore, the stability of doped systems is examined by the binding energy, and the nearest-neighbor distances between the Sb and dopants (d_1 and d_2) are also summarized in Table 1. The negative binding energies of doped systems indicate the stable geometry structures, and the Ti-Sb is the most stable with a binding energy of -6.40 eV. Moreover, we illustrate one type of optimized doped geometry structures in Fig. 2, namely, Ge-Sb. As shown in Fig. 2 and Table 1, after the doping of Ge, there is no obvious distortion appears

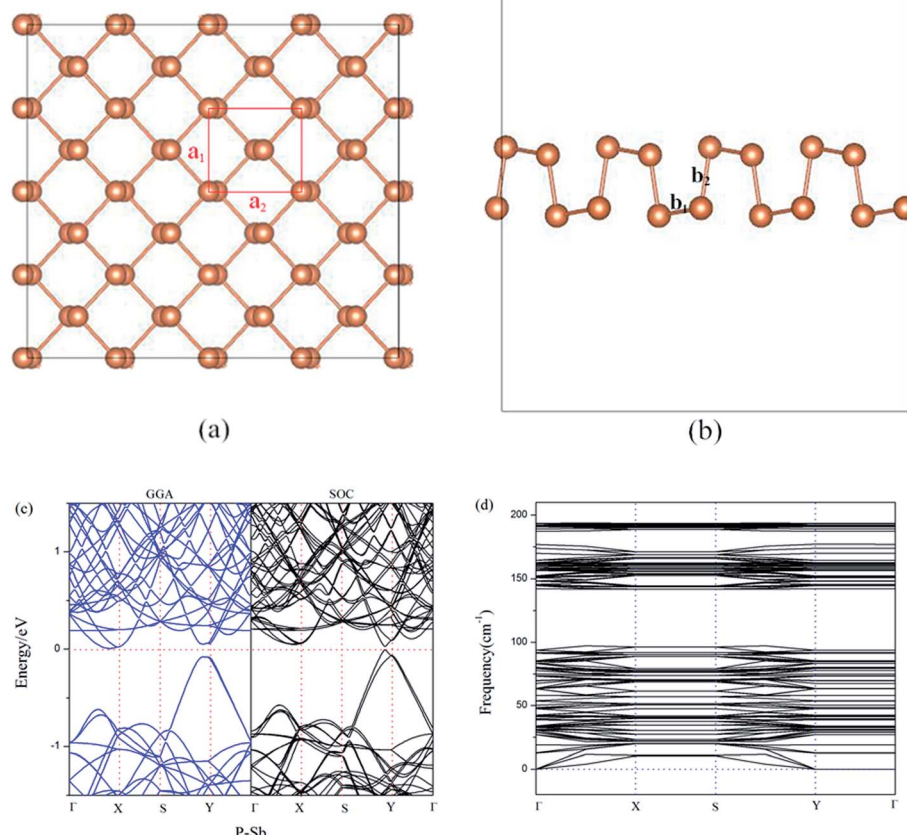


Fig. 1 The top (a) and side (b) view of the optimized structure of pristine antimonene. (c) Band structure and (d) phonon dispersion curves structure of pristine antimonene.



Table 1 Summary of results for doped aW-Sb systems. The properties performed are the nearest band length of the dopant to the two adjacent Sb atom (d_1 and d_2), the binding energy (E_b), the total magnetic moment of doped systems (M_{total}), and the charge transfers of dopants (Q)

Adatom	d_1 (Å)	d_2 (Å)	E_b (eV)	M_{total} (μ_B)	Q (e)
Ge	2.72	2.76	-3.51	0	-0.30
Se	2.76	2.67	-3.51	0	-0.53
Sn	2.91	2.98	-3.24	0	0.18
Te	2.94	2.86	-2.83	0	-0.27
Sc	3.03	2.87	-5.80	0	0.37
Ti	2.87	2.72	-6.40	1.0	0.89
V	2.75	2.67	-5.08	2.7	0.68
Cr	2.73	2.67	-3.75	3.2	0.45
Mn	2.73	2.71	-3.96	3.7	0.42
Fe	2.57	2.50	-4.82	1.3	-0.13
Co	2.49	2.47	-5.88	0	-0.36
Ni	2.55	2.50	-5.70	0	-0.31

and the value of b_1 (2.93 Å) and b_2 (2.87 Å) in pristine aW-Sb change to be 2.72 Å and 2.76 Å. The change of bond lengths of b_1 varied in 0.01–0.44 Å, when that of b_2 is 0.00–0.40 Å. Among the doped structures, the decrease of bond length in Co-Sb was the most obvious. Furthermore, the charge transfer of dopant is calculated by Bader charge analysis.³⁹ The result indicates that Ge, Se, and Te act as acceptors, while the other dopants are donors. The large charge transfer between the dopants and aW-Sb substrate indicated the strong interaction present, and the Ti-dopant exhibits 0.89e, which is the largest value of Q and is agreement with its largest binding energy. Therefore, the small change of geometry structures, large binding energies and charge transfer are all imply the stability of doped systems.

3.2 Electronic and magnetic properties

To further understand the effect of dopants on the electronic and magnetic structures, we further illustrate the band structure and projected density of states (PDOS) of all doped-Sb systems in Fig. 3 and 4. As performed in Fig. 3, the black and blue color lines represent spin-up and spin-down channels for the PBE results. The PBE results exhibit blue color, when the spin-up and spin-

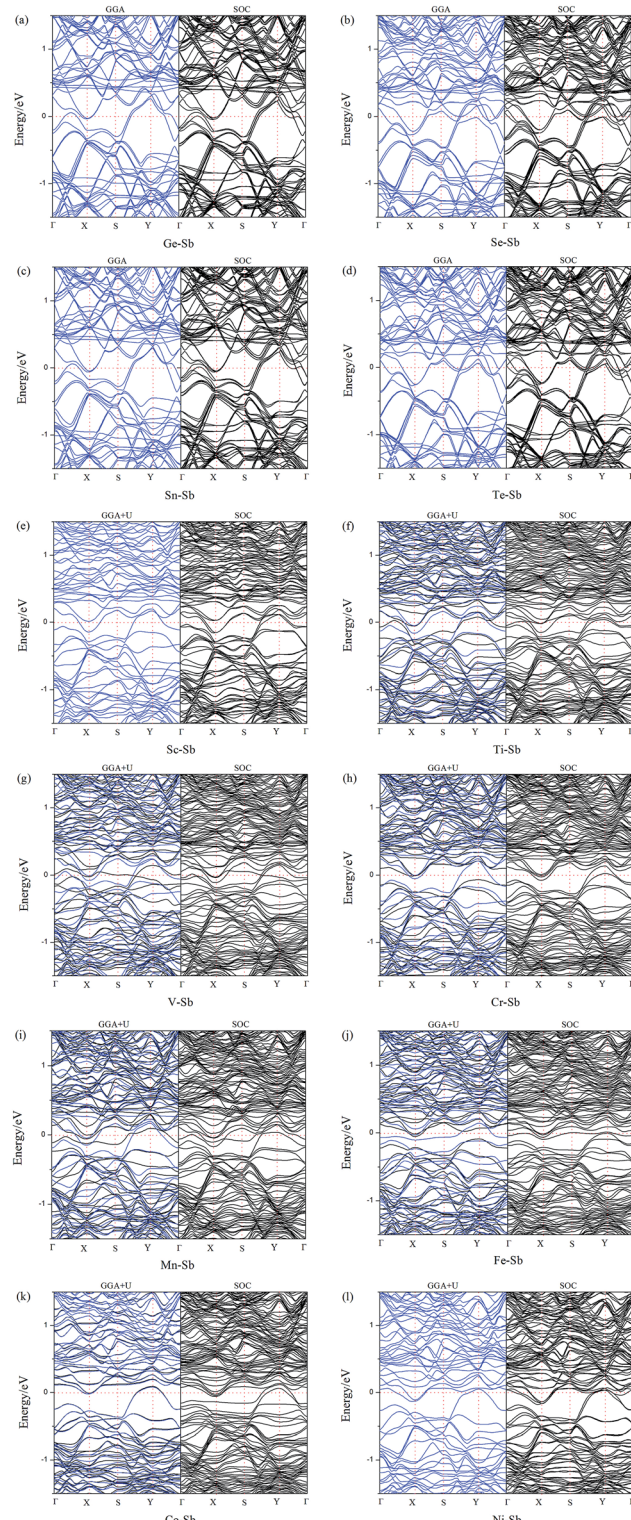


Fig. 3 Band structures of (a) Ge–Sb, (b) Se–Sb, (c) Sn–Sb, (d) Te–Sb, (e) Sc–Sb, (f) Ti–Sb, (g) V–Sb, (h) Cr–Sb, (i) Mn–Sb, (j) Fe–Sb, (k) Co–Sb, and (l) Ni–Sb. For the GGA+U or GGA band structure results, the black and blue colors represent spin-up and spin-down channels, respectively.

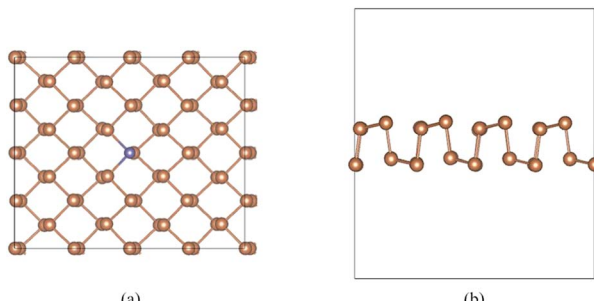


Fig. 2 The top (a) and side (b) view of the optimized structure of Ge-doped antimonene.

down bands are coincident. We first discuss the GGA (GGA+U) results. As shown in Fig. 3, the doped aW-phase antimonene exhibit metallic, due to the appearance of impurity-band around



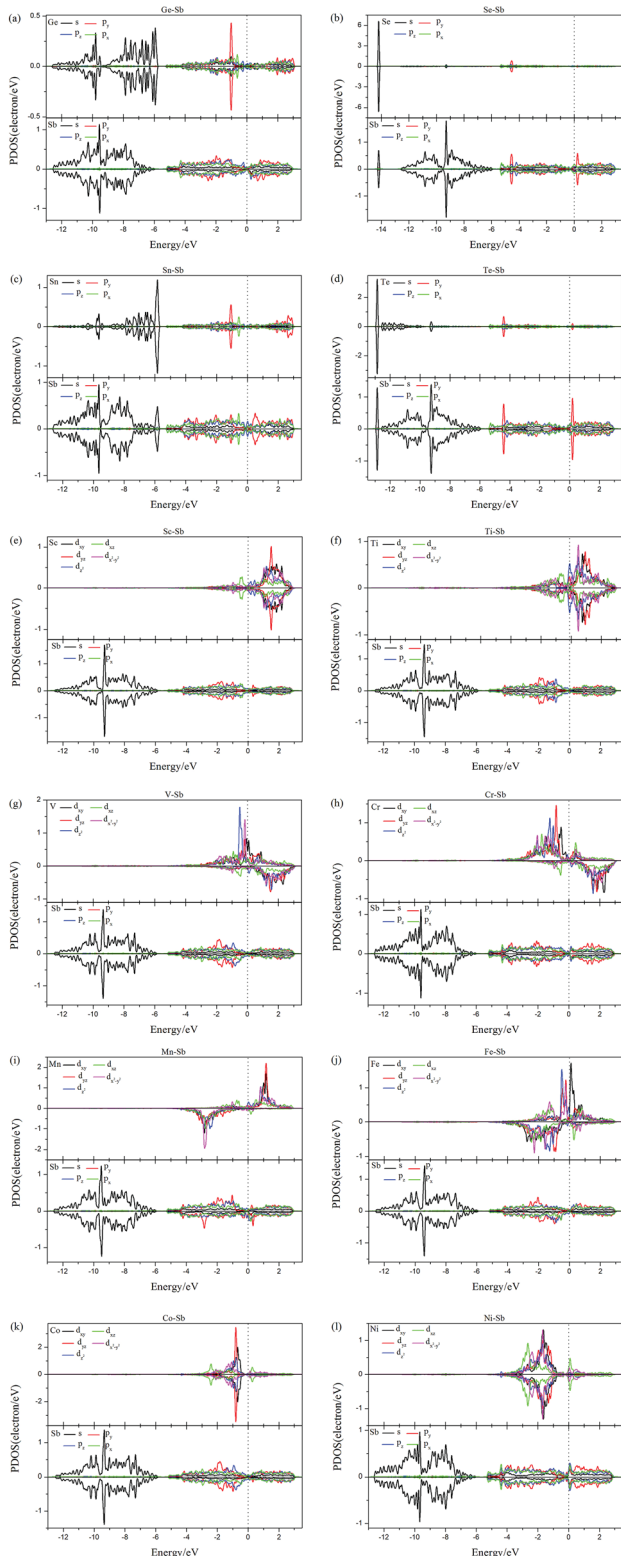


Fig. 4 The PDOS of the dopants and the adjacent Sb atoms around the dopants: (a) Ge–Sb, (b) Se–Sb, (c) Sn–Sb, (d) Te–Sb, (e) Sc–Sb, (f) Ti–Sb, (g) V–Sb, (h) Cr–Sb, (i) Mn–Sb, (j) Fe–Sb, (k) Co–Sb, and (l) Ni–Sb.

the Fermi level contributed by the dopant. We can classify the systems into two types, including weak conductivity and strong conductivity structures. It can be found that only a few channels

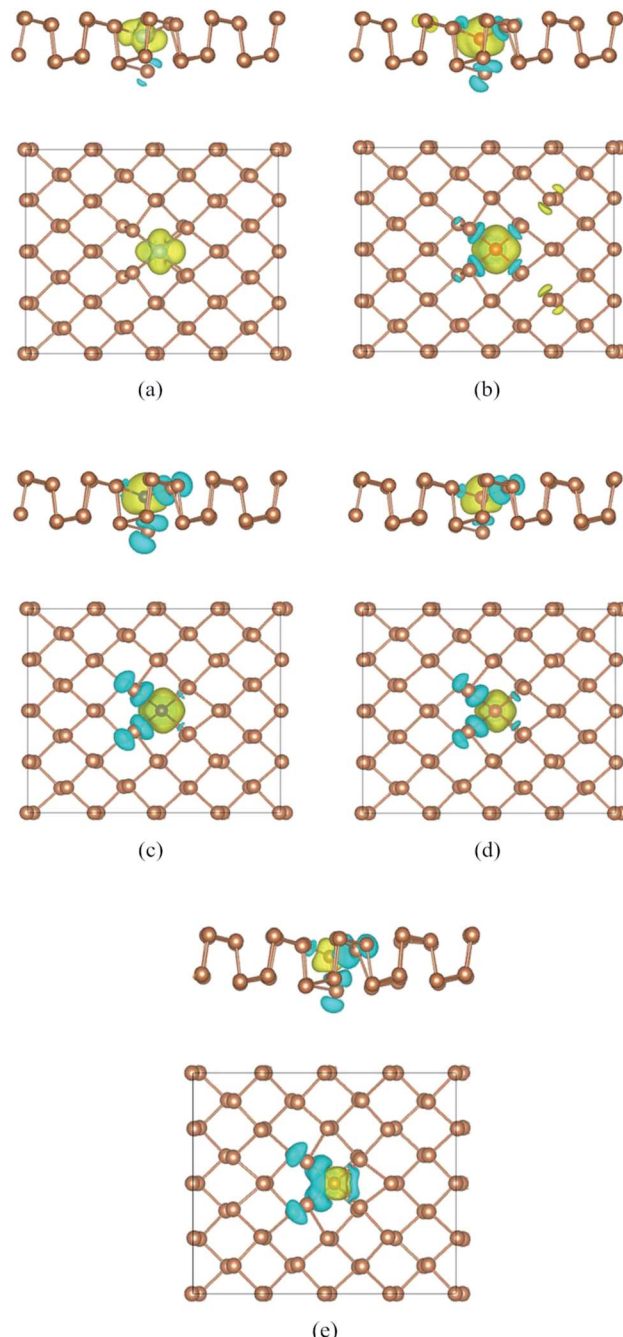


Fig. 5 Top view of spin density of doped antimonene: (a) Ti–Sb, (b) V–Sb, (c) Cr–Sb, (d) Mn–Sb, and (e) Fe–Sb. The isosurface value is set to be $0.0015e \text{ \AA}^{-1}$.

of valence or conductive bands go through the Fermi level in Fig. 3(e)–(l) and then the Sc-, Ti-, V-, Cr-, Mn-, Fe-, Co-, and Ni-doped antimonene exhibit weak conductive character. Although, there are more bands through the Fermi level in the Ge-, Se-, Sn-, and Te-doped systems, indicating a character of relative strong conductivity. The pristine aW-phase antimonene is nonmagnetic structure, while the doping of Ti, V, Cr, Mn, and Fe induced magnetic states. As performed Fig. 3(f)–(j), the spin-up and spin-down band channels are unsymmetrical, and we

summary the total magnetic moment of systems in Table 1. For the SOC results, it can be found that the splitting of electronic bands is not obvious, and the shapes of band structures of the doped systems with and without SOC are similar, which is in agreement with previous report.²²

Aiming to deeply explore the contribution of magnetic states, we illustrate the PDOS of dopants and the adjacent Sb atoms in Fig. 4. Firstly, there are obvious hybridization between the dopant and adjacent Sb atoms above and below the Fermi level, which is agreement with the large binding energies and charge transfers, indicating that chemical bonds form and the excellent stability of doped systems. Transition-metal (TM) is well known as magnetic metal. After doping of TM-dopants, the Sc-, Co-, Ni-doped antimonene still maintain nonmagnetic state. It may be resulted from the coupling of unpaired d-orbital electrons of TM-dopants and the p-orbital of adjacent Sb atoms, and that is consistent with the strong hybridization performed in Fig. 4. For the five types of magnetic structures, the d-orbital of dopants dominate the magnetic properties of structures. For example, the unsymmetrical sharp peaks of PDOS in Ti-Sb is mainly contributed by d_{xy} and d_{z^2} orbital, and the magnetic property of Mn-Sb system is dominated by $d_{x^2-y^2}$ and d_{yz} orbital.

To deeply explore the magnetic properties, we also perform the spin density distributions of Ti-Sb, V-Sb, Cr-Sb, Mn-Sb, and Fe-Sb systems in Fig. 5. Firstly, it is obvious that spin density is mainly localized at dopant and adjacent Sb atoms, and that is agreement with the PDOS result (Fig. 4). Secondly, the magnetic moments of dopant are contrary to the adjacent Sb atoms. According to our calculated results, the magnetic moments of Ti-, V-, Cr-, Fe-, and Mn-dopant are $1.1 \mu_B$, $2.8 \mu_B$, $3.4 \mu_B$, $4.1 \mu_B$, and $2.3 \mu_B$, while the total magnetic moments of doped structures are $1.0 \mu_B$, $2.7 \mu_B$, $3.2 \mu_B$, $3.7 \mu_B$, and $1.3 \mu_B$ (Table 1). Therefore, the doping could produce interesting magnetic properties in nonmagnetic aW-phase antimonene.

4. Conclusions

In summary, the geometry stability, electronic and magnetic properties of doped aW-phase antimonene (aW-Sb) have been systematically explored by using density functional theory (DFT) method. The large binding energies and charge transfer between the dopant and antimonene substrate indicate the stable geometry structures of doped systems. The pristine aW-Sb is nonmagnetic semiconductor with a narrow bandgap. After doping, the doped aW-Sb structures all exhibit metallic, and the V-, Cr-, Mn-, Fe-doped systems exhibited different magnetic properties. According to the results of PDOS and spin density distribution, it can be found that the dopant and adjacent Sb atoms dominate the magnetic behavior. Our result is expected to promote the application of antimonene in nanoelectronic devices.

Conflicts of interest

There are no conflicts to declare.

Acknowledgements

This work is supported by National Natural Science Foundation of China (NSFC, Grant No. 11604080 and 61874160), and the Student Research Training Program of School of Physics and Engineering (Grant No. WLSRTP201908).

References

- 1 D. Xiao, G. B. Liu, W. Feng, X. Xu and W. Yao, Coupled Spin and Valley Physics in Monolayers of MoS₂ and Other Group-VI Dichalcogenides, *Phys. Rev. Lett.*, 2012, **108**, 196802.
- 2 Z. Y. Zhu, Y. C. Cheng and U. Schwingenschlögl, Giant spin-orbit-induced spin splitting in two-dimensional transition-metal dichalcogenide semiconductors, *Phys. Rev. B: Condens. Matter Mater. Phys.*, 2011, **84**, 153402.
- 3 W. Qing Hua, K. Z. Kourosh, K. Andras, J. N. Coleman and M. S. Strano, Electronics and optoelectronics of two-dimensional transition metal dichalcogenides, *Nat. Nanotechnol.*, 2012, **7**, 699–712.
- 4 H. Shu, P. Luo, P. Liang, D. Cao and X. Chen, Layer-Dependent Dopant Stability and Magnetic Exchange Coupling of Iron-Doped MoS₂ Nanosheets, *ACS Appl. Mater. Interfaces*, 2015, **7**, 7534–7541.
- 5 D. Cao, T. Shen, P. Liang, X. Chen and H. Shu, Role of Chemical Potential in Flake Shape and Edge Properties of Monolayer MoS₂, *J. Phys. Chem. C*, 2015, **119**, 4294–4301.
- 6 A. A. Kistanov, A. R. Davletshin, S. V. Ustuzhanina, I. Evazzade, D. Saadatmand, S. V. Dmitriev and E. A. Korznikova, Effects of substrate and environmental adsorbates on the electronic properties and structural stability of antimonene, *J. Mater. Sci.*, 2018, **53**, 15559–15568.
- 7 S. Zhang, S. Guo, Z. Chen, Y. Wang, H. Gao, J. Gómez-Herrero, P. Ares, F. Zamora, Z. Zhu and H. Zeng, Recent progress in 2D group-VA semiconductors: from theory to experiment, *Chem. Soc. Rev.*, 2018, **47**, 982–1021.
- 8 T. P. Kaloni, G. Schreckenbach and M. S. Freund, Large Enhancement and Tunable Band Gap in Silicene by Small Organic Molecule Adsorption, *J. Phys. Chem. C*, 2014, **118**, 23361–23367.
- 9 E. C. Anota, M. S. Villanueva, A. E. Morales and M. Castro, Stability, electronic and magnetic properties of the Octagraphene-like boron nitride Nanosheets: in silico studies, *Fullerenes, Nanotubes, Carbon Nanostruct.*, 2018, **26**, 93–99.
- 10 R. G. Amorim and R. H. Scheicher, Silicene as a new potential DNA sequencing device, *Nanotechnology*, 2015, **26**, 154002.
- 11 S. Zhang, Z. Yan, Y. Li, Z. Chen and H. Zeng, Atomically Thin Arsenene and Antimonene: Semimetal–Semiconductor and Indirect–Direct Band-Gap Transitions, *Angew. Chem., Int. Ed.*, 2015, **54**, 3112–3115.
- 12 T. Lei, C. Liu, J.-L. Zhao, J.-M. Li, Y.-P. Li, J.-O. Wang, R. Wu, H.-J. Qian, H.-Q. Wang and K. Ibrahim, Electronic structure of antimonene grown on Sb₂Te₃ (111) and Bi₂Te₃ substrates, *J. Appl. Phys.*, 2016, **119**, 015302.



13 P. Ares, F. Aguilar-Galindo, D. Rodríguez-San-Miguel, D. A. Aldave, S. Díaz-Tendero, M. Alcamí, F. Martín, J. Gómez-Herrero and F. Zamora, Mechanical Isolation of Highly Stable Antimonene under Ambient Conditions, *Adv. Mater.*, 2016, **28**, 6332–6336.

14 A. V. Krasheninnikov, P. O. Lehtinen, A. S. Foster, P. Pyykko and R. M. Nieminen, Embedding transition-metal atoms in graphene: structure, bonding, and magnetism, *Phys. Rev. Lett.*, 2009, **102**(12), 126807.

15 H. Bing, X. Hongjun, Y. Jaejun and W. Su-Huai, Effective control of the charge and magnetic states of transition-metal atoms on single-layer boron nitride, *Phys. Rev. Lett.*, 2012, **108**, 206802.

16 D. Ma, W. Ju, T. Li, X. Zhang, C. He, B. Ma, Y. Tang, Z. Lu and Z. Yang, Modulating electronic, magnetic and chemical properties of MoS₂ monolayer sheets by substitutional doping with transition metals, *Appl. Surf. Sci.*, 2016, **364**, 181–189.

17 L. Hu, X. Hu, X. Wu, C. Du, Y. Dai and J. Deng, Density functional calculation of transition metal adatom adsorption on graphene, *J. Phys.: Condens. Matter*, 2008, **405**, 3337–3341.

18 M. Dongwei, L. Zhansheng, J. Weiwei and T. Yanan, First-principles studies of BN sheets with absorbed transition metal single atoms or dimers: stabilities, electronic structures, and magnetic properties, *J. Phys.: Condens. Matter*, 2012, **24**, 145501.

19 X. Q. Wang, W. G. Chen, Z. L. Zhu and Y. Jia, Electronic and Magnetic Properties Modulated by Adsorption of 3 d Transition Metal Atoms in Monolayer and Bilayer MoS₂ Sheets, *Acta Metall. Sin. (Engl. Lett.)*, 2015, **28**, 793–798.

20 M. Y. Liu, Q. Y. Chen, Y. Huang, Z. Y. Li, C. Cao and Y. He, Electronic and magnetic properties of 3D transition-metal atom adsorbed arsenene, *Nanotechnology*, 2018, **29**, 095203.

21 S. Dai, W. Zhou, Y. Liu, Y.-L. Lu, L. Sun and P. Wu, Tunable electronic and magnetic properties of antimonene system via Fe doping and defect complex: a first-principles perspective, *Appl. Surf. Sci.*, 2018, **448**, 281–287.

22 C. He, M. Cheng and W. Zhang, Tunable electronic and magnetic properties of transition metals doped antimonene: a first-principles study, *Mater. Res. Express*, 2018, **5**, 065059.

23 Z. Yungang and L. Xudong, Effects of interstitial dopings of 3 d transition metal atoms on antimonene: a first-principles study, *Appl. Surf. Sci.*, 2018, **458**, 572–579.

24 T. T. Li, C. He and W. X. Zhang, Electric field improved the sensitivity of CO on substitutionally doped antimonene, *Appl. Surf. Sci.*, 2018, **427**, 388–395.

25 L. F. Yang, Y. Song, W. B. Mi and X. C. Wang, Prediction of spin-dependent electronic structure in 3d-transition-metal doped antimonene, *Appl. Phys. Lett.*, 2016, **109**, 022103.

26 L. F. Yang, Y. Song, W. B. Mi and X. C. Wang, The electronic structure and spin-orbit-induced spin splitting in antimonene with vacancy defects, *RSC Adv.*, 2016, **6**, 66140–66146.

27 G. Kresse, Ab initio molecular dynamics for liquid metals, *Phys. Rev. B: Condens. Matter Mater. Phys.*, 1993, **48**, 13115–13118.

28 G. Kresse and J. Furthmüller, Efficiency of ab-initio total energy calculations for metals and semiconductors using a plane-wave basis set, *Comput. Mater. Sci.*, 1996, **6**, 15–50.

29 G. Kresse and J. Furthmüller, Efficient iterative schemes for ab initio total-energy calculations using a plane-wave basis set, *Phys. Rev. B: Condens. Matter Mater. Phys.*, 1996, **54**, 11169–11186.

30 J. P. Perdew, K. Burke and M. Ernzerhof, Generalized Gradient Approximation Made Simple, *Phys. Rev. Lett.*, 1996, **77**, 3865–3868.

31 G. Kresse and D. Joubert, From ultrasoft pseudopotentials to the projector augmented-wave method, *Phys. Rev. B: Condens. Matter Mater. Phys.*, 1999, **59**, 1758–1775.

32 G. Stefan, Semiempirical GGA-type density functional constructed with a long-range dispersion correction, *J. Comput. Chem.*, 2010, **27**, 1787–1799.

33 Y. Song, X. C. Wang and W. B. Mi, Spin splitting and electric field modulated electron-hole pockets in antimonene nanoribbons, *npj Quantum Mater.*, 2017, **2**, 15.

34 W. W. Ju, D. H. Wang, T. W. Li and S. J. Gong, Electric field control of Rashba spin splitting in 2D N^{III}X^{VI}(N = Ga, In; X = S, Se, Te) monolayer, *J. Phys.: Condens. Matter*, 2020, **32**, 175503.

35 D. Singh, S. K. Gupta, Y. Sonvane and I. Lukačević, Antimonene: a monolayer material for ultraviolet optical nanodevices, *J. Mater. Chem. C*, 2016, **4**, 6386–6390.

36 G. Wang, R. Pandey and S. P. Karna, Atomically Thin Group V Elemental Films: Theoretical Investigations of Antimonene Allotropes, *ACS Appl. Mater. Interfaces*, 2015, **7**, 11490–11496.

37 O. Üzengi Aktürk, E. Aktürk and S. Ciraci, Effects of adatoms and physisorbed molecules on the physical properties of antimonene, *Phys. Rev. B*, 2016, **93**, 035450.

38 O. Ü. Aktürk, V. O. Özçelik and S. Ciraci, Single-layer crystalline phases of antimony: Antimonenes, *Phys. Rev. B: Condens. Matter Mater. Phys.*, 2015, **91**, 235446.

39 W. Tang, E. Sanville and G. Henkelman, A grid-based Bader analysis algorithm without lattice bias, *J. Phys.: Condens. Matter*, 2009, **21**, 084204.

